Journal of Applied Fluid Mechanics, Vol. 11, No. 4, pp. 1033-1045, 2018.
Available online at www.jafmonline.net, ISSN 1735-3572, EISSN 1735-3645.
DOI: 10.29252/jafm.11.04.27943

Reduced-Order Modeling of Unsteady Hypersonic Aerodynamics in Multi-Dimensional Parametric Space

Z. Chen, Y. Zhao† and R. Huang

State Key Laboratory of Mechanics and Control of Mechanical Structures, Nanjing University of Aeronautics and Astronautics, 210016 Nanjing, People's Republic of China

†*Corresponding Author Email: zyhae@nuaa.edu.cn*

(Received May 3, 2017; accepted January 27, 2018)

ABSTRACT

A novel reduced order model (ROM) for unsteady hypersonic aerodynamics is developed, which is applicable for the variations of multi-parameters. The key to the developed ROM lies in the CFD-based model reduction of the steady aerodynamic component, which stems from the quasi-steady nature of aerodynamic forces in the hypersonic regime. Concretely, the proper orthogonal decomposition (POD) method, combined with Kriging interpolation, is used to construct the ROM for the steady aerodynamic component; meanwhile the unsteady part is directly obtained from Donov's third-order piston theory. The new procedure is applied to a three-dimensional low aspect ratio wing (Lockheed F-104 Starfighter wing). It is shown that the developed ROM is able to accurately predict the unsteady hypersonic aerodynamic loads over a wide range of different flight conditions compared with the direct CFD computation.

Keywords: Reduced order model; Proper orthogonal decomposition; Kriging surrogate; Piston theory; Multi-dimensional parametric space.

NOMENCLATURE

a_∞	speed of sound	$\mathbf{U}_i$	POD mode
a_r	coefficient of the rth POD mode	$\mathbf{V}$	matrix of eigenvectors
$\mathbf{C}$	covariance matrix	$\mathbf{v}_i$	eigenvector of covariance matrix
C_p	pressure coefficient	v_n	normal velocity of the surface
C_p^{ROM}	pressure coefficient of reduced order model	w	midsurface displacement of the surface
$C_{p,s}$	steady component of piston theory pressure	$\mathbf{x}$	sampling point
$C_{p,s}^{ROM}$	steady component of reduced order model	x_{rot}	x coordinate value of the midchord
$C_{p,\text{v}}$	component of piston theory pressure due to surface velocity	Z	instantaneous surface position
$\bar{C}_p$	component of piston theory pressure due to combined surface velocity and surface inclination	Z_h	thickness distribution of the surface
$C_{p,us}^{PT}$	unsteady component of piston theory pressure	α	angle of attack
f_j	polynomial function	β	side-slip angle
L_1	normalized root mean square error	Φ	structural mode shape
M	number of sampling points	Φ_r	nonlinear function
Ma_∞	freestream Mach number	$\hat{\Phi}_r$	kriging approximation
N	number of nodes of aerodynamic mesh	γ	radio ratio of the specific heat ratio of air
$\mathbf{P}$	snapshot matrix	λ_i	eigenvalue of covariance matrix
$\bar{\mathbf{p}}$	average vector of pressure	ρ_∞	air density of the freestream
p	pressure of of the surface	σ_i	singular value
p_∞	pressure of the freestream		

1. INTRODUCTION

Hypersonic vehicles generally refer to the flight of vehicles in an atmosphere layer or trans-atmosphere layer at a Mach number above 5. The hypersonic vehicle, such as an X-43, usually adopts a long, slender lifting body layout. The body and aerodynamic control surfaces are flexible due to minimum-weight restrictions. Due to complex interactions between the flow, flight dynamics, structural response, controllers, and propulsion system, the aeroelastic and aerothermoelastic properties of the hypersonic vehicle are very important (McNamara, 2008, 2011), and it is impractical to test these properties in wind-tunnels. Therefore, accurate prediction of the unsteady aerodynamic loads becomes one of the primary challenges for the design of hypersonic vehicles.

Limited by the capabilities of computational facilities, early researchers of hypersonic aeroelasticity had to employ a number of approximate unsteady aerodynamic models, such as piston theory (Liu, 1997) and (Dowell, 2016), Newtonian impact theory, and the shock-expansion theory (McNamara, 2010). The advantages of high computational efficiency and ease of implementation make these analytical models very attractive at the stage of preliminary design. However, these analytical models neglect some potential important effects (viscidity and real gas effects, etc.), and it is difficult to accurately predict aerodynamic loads under some complex flow conditions. Furthermore, the aerodynamic forces in the hypersonic regime are quite large, and any inaccurate prediction of these loads may lead to an unreliable design of the control system, which could result in air accidents. Recently, along with the rapid development of the CFD technique, Euler and Navier-Stokes (N-S) equations have been used to accurately predict unsteady aerodynamic loads (Boulahia, 2014). This makes the direct CFD/CSD coupling computations possible in the time domain. Full-order CFD models, also known as high-fidelity models, can provide the necessary accuracy for aeronautical applications (McNamara, 2008). However, the direct CFD computation is very time consuming, and it is unsuitable for design processes such as aeroelastic tailoring, which requires iterative computations in multi-dimensional parameter space. In addition, CFD simulations in the time domain will produce a huge amount of input and output time histories, so they are also unsuitable for analysis or synthesis problems of the control system. Consequently, accurate lower-dimensional models, also known as ROMs, that can capture the dominant behavior of the system of interest, are often sought to enable real-time operations by practitioners (Skujins, 2011), (Kim, 2015) and (Huang, 2014).

A number of ROMs have been proposed to improve the efficiency of CFD. The overviews of different ROMs are discussed by Ghoreyshi *et al*. (2014) and Lucia *et al* (2004). ROMs seek to construct a lower-dimensional model by extracting information from a limited number of full-order simulations. POD (Hall, 2000); (Thomas, 2010); (Lieu, 2007) and surrogate-based approaches (Glaz, 2010); (Liu, 2016) are two typical representatives of such ROMs. The POD approach essentially belongs to a type of projection-based model reduction methods by projecting the high-fidelity model onto a well-chosen subspace consisting of a set of basis vectors. Kriging is an interpolation method that is well suited for approximating nonlinear functions. However, the above ROMs for unsteady aerodynamics are built on one operating point (fixed flight conditions) and are not effective on other points. A new ROM must be reconstructed with the variations of the operating point, even for a tiny change.

In general, the aeroelastic analysis and tailoring, control, and many other applications involve several parameter changes, for example, variations in shape, Mach number, angle of attack, etc. Hypersonic vehicles operate within a large range of flight envelopes and undergo large variations in dynamic parameters. Therefore, it is an urgent requirement to establish an efficient ROM, that is applicable for the variations of multi-parameters. A survey of model reduction methods for parametric dynamical systems is given in (Benner, 2013), where various methods are presented and compared. A parametric reduced-order modeling approach has been introduced to efficiently generate ROMs that are accurate over a broad range of parameters, without the need for a new reduction model at each design point. To solve the ROM adaptation issue, several POD-based ROMs have been proposed. Schmidt *et al*. (2004) developed a global POD (GPOD) method by enriching the snapshot matrix with solutions corresponding to different values of the varied parameters. The major drawback of this approach lies in the lack of the optimal approximation property of the POD method, which usually results in an unsuccessful ROM adaptation in the transonic regime (Amsallem, 2008). The direct interpolation method (Lieu, 2004) attempts to construct a set of new reduced-order bases associated with a new set of physical parameters by interpolating pre-computed reduced-order bases. However, the obtained bases are not guaranteed to be orthogonal. Subspace angle interpolation has been used for F-16 aeroelastic simulations (Lieu, 2007), when the freestream Mach number or angle of attack is varied. However, the subspace angle interpolation approach has proven difficult to extend for variations of more than one parameter.

In this work, a parametric ROM for hypersonic unsteady aerodynamics is developed, which is based on the following three conditions: quasi-steady nature of the hypersonic flow, the high computational efficiency of the piston theory, and the need for ROM adaptation in multi-dimensional parameter space. A flow is said to be quasi-steady when the reduced frequency is small ($k \ll 1$). This condition occurs if the frequencies are very low, the vehicle semichord is very small, or the velocity is very high. For hypersonic flows (Scott, 1996), the fluid solution is quasi-steady. The developed ROM includes the ROM for steady aerodynamic components and the unsteady component from Donov's third-order formulation of piston theory, which is denoted here as the PT-ROM method. A steady aerodynamic ROM is constructed to give the accurate steady aerodynamic component in multi-parameter space by combining the POD method with the Kriging surrogate. Three sections in this paper discuss the PT-ROM method in detail. In the section 2, the relevant theories regarding the PT-ROM method are briefly described: piston theory, Latin hypercube sampling, proper orthogonal decomposition (POD) and surrogate models (Kriging model), and the implementation steps of the PT-ROM method are discussed in detail, and two separate error metrics are

defined to judge the accuracy of the PT-ROM compared with the CFD. In the section 3, the validity of the PT-ROM method is verified by simulation results on a low-aspect-ratio wing over multidimensional parameter space. Finally, concluding remarks are made in section 4.

2. PARAMETRIC REDUCED-ORDER MODELING APPROACH FOR UNSTEADY HYPERSONIC AERODYNAMICS

Figure 1 shows the schematic diagram of the PT-ROM framework. First, the input parameter space (Mach number, angle of attack, slide-slip angle, etc.) with bounds is given. Then, Latin hypercube sampling (LHS) is used to identify a set of sampling points. The basic function of the PT-ROM is to correct the classical piston theory using CFD computations. For this purpose, the classical piston theory is decomposed into the steady component (value-dependent) and the unsteady component (rate-dependent). The steady component can be replaced by the result of steady-state CFD flow analysis. Based on steady-state CFD results, POD and Kriging surrogates are employed to construct an efficient parametric ROM. Combining the steady aerodynamic ROM with the unsteady component of Donov's piston theory, the parametric PT-ROM is obtained.

2. 1 Donov's Third-Order Piston Theory Including Side-Slip Angle

The piston theory (Ashkey, 1956) is a technique that has been used to predict the unsteady aerodynamic forces on a lifting surface when the Mach number is sufficiently high. The piston theory assumes that for a thin or slender body, the gradients of flow parameters in the direction of the free stream are negligible compared to the gradients

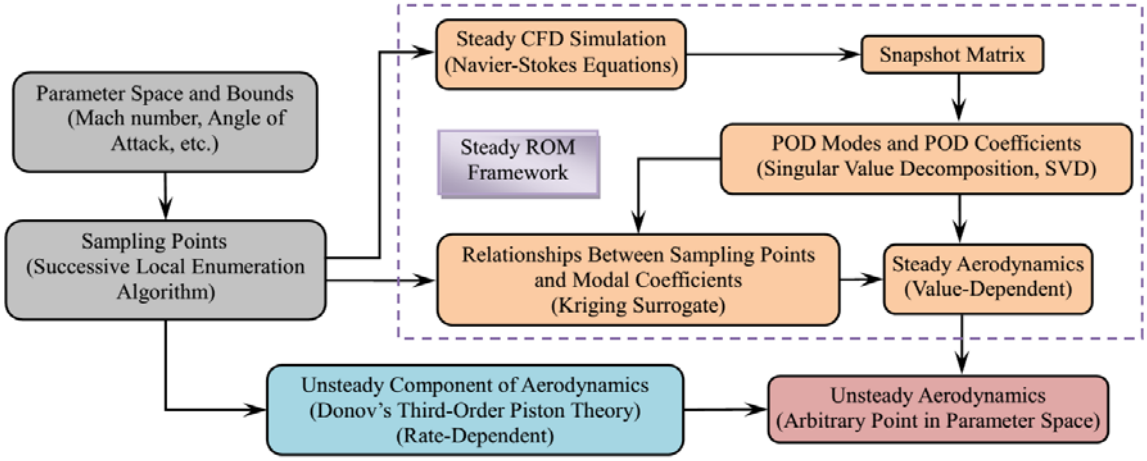

Fig. 1. Schematic diagram of the unsteady aerodynamic PT-ROM.

the normal to the surface, and the interaction of arbitrary two points on the surface is very small. This characteristic of the flow can be simply mimicked by a moving piston in a one-dimensional channel, as shown in Fig. 2.

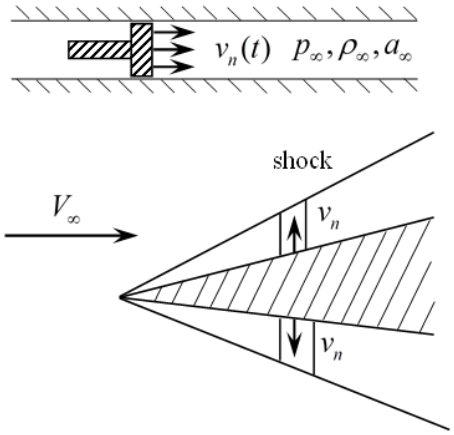

Fig. 2. Pressure on a surface can be mimicked by a moving piston in a one-dimensional channel.

The classical piston theory yields the following formula for local pressure p of the surface:

$$p = p_\infty \left(1 + \frac{\gamma - 1}{2}\frac{v_n}{a_\infty}\right)^{\frac{2\gamma}{\gamma-1}} \tag{1}$$

where γ is the radio ratio of the specific heat ratio of air, and v_n is the normal velocity of the surface such that

$$v_n = \frac{\partial Z(x,y,t)}{\partial t} + V_\infty \left\{\frac{\partial Z(x,y,t)}{\partial \xi}\right\} \tag{2}$$

As shown in Fig. 3, the all-moving lifting surface (control surface) is considered. The instantaneous lifting surface position can be written as

$$Z(x,y,t) = w(x,y,t) + Z_h(x,y) + \alpha(t)(x_{\text{rot}} - x) \tag{3}$$

where $w(x,y,t)$ is the midsurface displacement of the control surface. $Z_h(x,y)$ is the thickness distribution. $\alpha(t)$ is the rotation of the control surface about the midchord at the root of the wing, and x_{rot} is the x coordinate value of the midchord.

For hypersonic aeroelastic applications, such as panel flutter, the side-slip angle is an important parameter influencing flutter speed and mode shape at the flutter point. In Fig. 3, the airstream coordinate system $\xi O \eta$ is

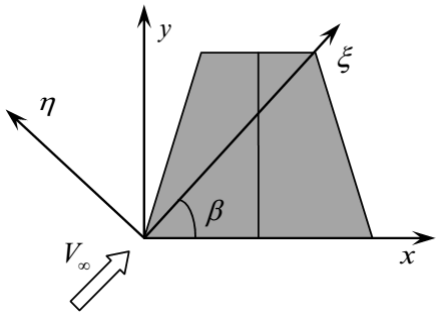

Fig. 3. Definition of side-slip angle β.

defined, and the axis ξ corresponds to the direction of the freestream. Note that the following relationship holds true

$$x = \xi\cos\beta - \eta\sin\beta\ ,\ y = \eta\cos\beta + \xi\sin\beta \tag{4}$$

Thus, we have

$$\frac{\partial Z(x,y,t)}{\partial\xi} = \frac{\partial Z}{\partial x}\frac{\partial x}{\partial\xi} + \frac{\partial Z}{\partial y}\frac{\partial y}{\partial\xi} = \frac{\partial Z}{\partial x}\cos\beta + \frac{\partial Z}{\partial y}\sin\beta \tag{5}$$

For $|v_n| << a_\infty$, we can expand the right hand side of Eq. (1) into the series expressed in terms of v_n / a_∞:

$$p = p_\infty + \rho_\infty a_\infty^2\left[c_1\frac{v_n}{a_\infty} + c_2\left(\frac{v_n}{a_\infty}\right)^2 + c_3\left(\frac{v_n}{a_\infty}\right)^3\right] \tag{6}$$

where $c_1 = 1$, $c_2 = (\gamma+1)/4$, $c_3 = (\gamma+1)/12$. Then, the pressure coefficient on an oscillating surface is given by

$$C_p = \frac{2}{Ma_\infty^2}\left[c_1\frac{v_n}{a_\infty} + c_2\left(\frac{v_n}{a_\infty}\right)^2 + c_3\left(\frac{v_n}{a_\infty}\right)^3\right] \tag{7}$$

Donov (1956) obtained a series expansion solution up to the fourth-order term, accounting separately for the isentropic part and the rotational part due to a simple wave and shock wave, respectively. Donov's third-order piston theory can be expressed as

$$C_p = \frac{2}{Ma_\infty^2}\left[c_1'\frac{v_n}{a_\infty} + c_2'\left(\frac{v_n}{a_\infty}\right)^2 + c_3'\left(\frac{v_n}{a_\infty}\right)^3\right] \tag{8}$$

where

$$c_1' = \frac{Ma_\infty}{\delta},\ c_2' = \frac{Ma_\infty^4(\gamma+1) - 4\delta^2}{4\delta^4},$$

$$c_3' = \frac{1}{6Ma_\infty\delta^7}\left(a_0Ma_\infty^8 + b_0Ma_\infty^6 + c_0Ma_\infty^4 + d_0Ma_\infty^2 + e_0\right)$$

$$a_0 = 3\left(\frac{\gamma+1}{4}\right)^2,\ b_0 = \frac{3\gamma^2 - 12\gamma - 7}{4},\ c_0 = \frac{9(\gamma+1)}{2},$$

$$d_0 = -6,\ e_0 = 4,\ \delta^2 = Ma_\infty^2 - 1$$

Substituting Eq. (2) into Eq. (8) yields the following pressure coefficient:

$$C_p(x,y,t) = C_{p,s}(x,y,t) + C_{p,v}(x,y,t) + \bar{C}_p(x,y,t) \tag{9}$$

where

$$C_{p,s}(x,y,t) = \frac{2c_1'}{Ma_\infty}\left(\frac{\partial Z}{\partial\xi}\right) + 2c_2'\left(\frac{\partial Z}{\partial\xi}\right)^2 + 2c_3'Ma_\infty\left(\frac{\partial Z}{\partial\xi}\right)^3 \tag{10}$$

$$C_{p,v}(x,y,t) = \frac{2c_1'}{Ma_\infty V_\infty}\left(\frac{\partial Z}{\partial t}\right) + \frac{2c_2'}{V_\infty^2}\left(\frac{\partial Z}{\partial t}\right)^2 + \frac{2c_3'Ma_\infty}{V_\infty^3}\left(\frac{\partial Z}{\partial t}\right)^3 \tag{11}$$

$$\bar{C}_p(x,y,t) = \frac{4c_2'}{V_\infty}\left(\frac{\partial Z}{\partial t}\right)\left(\frac{\partial Z}{\partial\xi}\right) + \frac{6c_3'Ma_\infty}{V_\infty^2}\left(\frac{\partial Z}{\partial t}\right)^2\left(\frac{\partial Z}{\partial\xi}\right) \tag{12}$$

Equation (10) is the steady part, which is dependent on the surface instantaneous inclination, since the structure experiences transient rotations due to control input and elastic deformations. Equation (11) represents the component of pressure that is entirely dependent on the surface velocity. Equation (12), which represents the second- and third-order PT contributions to the wash-velocity terms, is dependent on the products of surface velocity and inclination.

For this approach, Eq. (10) is replaced with the steady-state pressure computed from a CFD flow analysis. Modification of the fluid mesh was completed before computing the full-order flow. To increase computational efficiency and ease of implementation, the steady-state CFD results are computed by constructing an ROM combining Kriging and POD in multidimensional parameter space.

2. 2 Steady Aerodynamics Modeling Via Parametric Reduced-Order Model

2. 2. 1 Sampling point selection

In the multi-parameter space, the principle of sampling point selection is that the characteristics of the model can be reflected by as few sampling points as possible. For this purpose, Latin hypercube sampling (LHS) is usually employed to select appropriate sampling points within the parameter space (Mackay, 2000).

The two main criteria for measuring sampling methods are the uniformity of space and projection. However, the sampling points generated by the standard LHS only ensure the projective property. In this paper, maximum LHS using the successive local enumeration (SLE) algorithm (Zhu, 2012) is used, which is an enhanced algorithm of the LHS. The goal of the SLE is to maximize the minimal distance, which is the minimum of all the distances between the point to be generated and the existing points. In Fig. 4, 100 sampling points are generated by LHS and SLE. It is shown that SLE is effective at generating sampling points with good space-filling and projective properties.

2.2.2 Proper Orthogonal Decomposition (POD)

POD is a mathematical technique that uses a set of optimal orthogonal basis functions to characterize the behavior of the full-system dynamics. The basic functions (called POD modes) are completely dependent on the experimental data or the results of high precision numerical simulations.

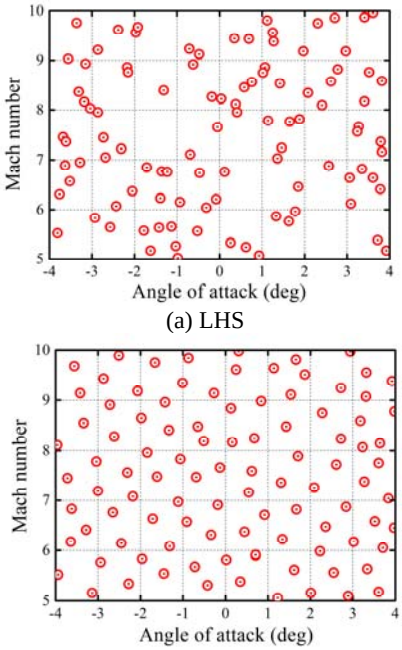

(a) LHS

(b) SLE

Fig. 4. Sampling points in 2-dimensional space using LHS and SLE

Consider a field vector $\mathbf{p}^{(k)}$ defined over a set of aerodynamic mesh points:

$$\mathbf{p}^{(k)} = (p_1^{(k)}, p_2^{(k)}, \cdots, p_N^{(k)})^{\mathrm{T}}, \quad k = 1, 2, \cdots, M \tag{13}$$

where M is the number of sampling points in the parameter space, and N is the number of nodes of aerodynamic mesh. The $N \times M$ matrix representing the sample of "snapshots" can be written as

$$\mathbf{P} = [\mathbf{p}^{(1)}, \mathbf{p}^{(2)}, \cdots \mathbf{p}^{(M)}] \tag{14}$$

The deviation matrix is defined as

$$\tilde{\mathbf{P}} = \mathbf{p}^{(k)} - \bar{\mathbf{p}}, \ k = 1, 2, \cdots, M \tag{15}$$

where $\bar{\mathbf{p}} = \frac{1}{M}\sum_{k=1}^{M} \mathbf{p}^{(k)}$ is the average vector. The singular value decomposition (SVD) of the covariance matrix $\mathbf{C} = \tilde{\mathbf{P}}^{\mathrm{T}}\tilde{\mathbf{P}}$ is given by

$$\mathbf{CV} = \mathbf{V}\mathrm{diag}[\lambda_1, \lambda_2, \cdots, \lambda_M] = \mathbf{V}\mathrm{diag}[\sigma_1^2, \sigma_2^2, \cdots, \sigma_M^2] \tag{16}$$

The covariance matrix $\mathbf{C}$ is a positive semi-definite matrix whose eigenvalues can be ordered in decreasing order such that $\lambda_1 \geq \lambda_2 \geq \cdots \geq \lambda_M = 0$, and the corresponding standard orthogonal eigenvector is given by $\mathbf{v}_1, \mathbf{v}_2, \cdots, \mathbf{v}_M$, $\mathbf{V} = [\mathbf{v}_1, \mathbf{v}_2, \cdots, \mathbf{v}_M]$. $\sigma_i = \sqrt{\lambda_i}, i = 1, 2, \cdots, M$ is the singular value of $\tilde{\mathbf{P}}^{\mathrm{T}}$. The orthonormal basis $\{\mathbf{U}_1, \mathbf{U}_2, \cdots, \mathbf{U}_{M-1}\}$ is given by

$$\mathbf{U}_i = \frac{\tilde{\mathbf{P}}\mathbf{v}_i}{\sqrt{\lambda_i}}, \ i = 1, 2, \cdots, M-1 \tag{17}$$

Therefore, the POD approximation of the snapshot solution is given by

$$\mathbf{p}^{(k)} = \bar{\mathbf{p}} + \sum_{i=1}^{m} a_i^{(k)} \mathbf{U}_i, \ m << M \tag{18}$$

with POD coefficients

$$a_i^{(k)} = \left\langle \mathbf{p}^{(k)} - \bar{\mathbf{p}}, \mathbf{U}_i \right\rangle_{L_2} = \frac{1}{\sqrt{\lambda_i}} (\mathbf{p}^{(k)} - \bar{\mathbf{p}})^{\mathrm{T}} \tilde{\mathbf{P}} \mathbf{v}_i \tag{19}$$

in which, $\langle \cdot, \cdot \rangle_{L_2}$ is the usual L_2 inner product.

2.2.3 Surrogate model

The goal of the surrogate model is to establish a simplified mathematical approximation. There exist a variety of approximation models (Gupta,2007) and (Skujins, 2014), such as the polynomial response surface, moving least square method, radial basis function, Kriging model and neural network. In this paper, the Kriging surrogate model, due to its outstanding ability to model the local behavior of the function, is used to establish the approximate relationships between POD coefficients and sampling points.

In multi-dimensional parametric space, a nonlinear functional relationship between POD coefficients and design variables is as follows:

$$a_r = \Phi_r(x_1, x_2, \cdots x_W), r = 1, 2, \cdots m \tag{20}$$

where a_r is the coefficient of the *r*th POD mode. The nonlinear function Φ_r can be approximated by using the surrogate model to obtain a surrogate mapping function $\hat{\Phi}_r$.

Consider the case of M sampling points $\mathbf{x}^{(1)}, \mathbf{x}^{(2)}, \cdots, \mathbf{x}^{(M)}$ in the W dimensional parameter space. The corresponding responses are denoted by $a_r^{(1)}, a_r^{(2)}, \cdots, a_r^{(M)}$. The Kriging approximation is expressed as at an arbitrary point $\mathbf{x}$:

$$\Phi_r(\mathbf{x}) = \sum_{j=1}^{N_0} \beta_j f_j(\mathbf{x}) + Z(\mathbf{x}) = \mathbf{f}^{\mathrm{T}}\boldsymbol{\beta} + Z \tag{21}$$

where $f_j(\mathbf{x})$, usually a polynomial function, are N_0 known regression models, β_j are the corresponding parameters, and $Z(\mathbf{x})$ is a stochastic process with mean zero and variance σ_{var}^2.

The covariance between the $Z(\mathbf{x})$ at two design points $\mathbf{x}^{(i)}$ and $\mathbf{x}^{(j)}$ is

$$Cov[Z(\mathbf{x}^{(i)}), Z(\mathbf{x}^{(j)})] = \sigma_{\mathrm{var}}^2 \mathbf{R}_{M \times M} \tag{22}$$

where $\mathbf{R}_{M \times M}$ is a correlation matrix, and $R_{ij} = R(\mathbf{x}^{(i)}, \mathbf{x}^{(j)})$ is a correlation function that depends on the relative location of these two design points. The Gaussian exponential correlation function is utilized in this paper. The covariance matrix is shown to be

$$R(\mathbf{x}^{(i)},\mathbf{x}^{(j)})=\prod_{k=1}^{W}\exp(-\theta_k\left|x_k^{(i)}-x_k^{(j)}\right|^{p_k}) \tag{23}$$

In the current study, the parameter p_k is fixed at the value of two; thus, the correlation function in Eq. (23) is related to the distance between the two design points. To find θ_k, the generalized least square estimates of β and σ_{var}^2, denoted by $\hat{\beta}$ and $\hat{\sigma}_{\text{var}}^2$, respectively, are employed:

$$\hat{\beta}=(\mathbf{F}^{\mathrm{T}}\mathbf{R}^{-1}\mathbf{F})\mathbf{F}^{\mathrm{T}}\mathbf{R}^{-1}\mathbf{y} \tag{24}$$

$$\hat{\sigma}_{\text{var}}^2=\frac{(\mathbf{y}-\mathbf{F}\hat{\beta})^{\mathrm{T}}\mathbf{R}^{-1}(\mathbf{y}-\mathbf{F}\hat{\beta})}{M} \tag{25}$$

where $\mathbf{F}$ can be defined as a $M\times N_0$ matrix where the ith row corresponds to the evaluation of the N_0 functions at the ith sampling point, and $\mathbf{y}$ is a $M\times 1$ vector of observed function outputs at the sampling points, which are expressed as

$$\mathbf{y}=\begin{bmatrix}a_r^{(1)}\\ a_r^{(2)}\\ \vdots\\ a_r^{(M)}\end{bmatrix},\mathbf{F}=\begin{bmatrix}f_1(\mathbf{x}^{(1)}) & f_2(\mathbf{x}^{(1)}) & \cdots & f_{N_0}(\mathbf{x}^{(1)})\\ f_1(\mathbf{x}^{(2)}) & f_2(\mathbf{x}^{(2)}) & \cdots & f_{N_0}(\mathbf{x}^{(2)})\\ \vdots & \vdots & \ddots & \vdots\\ f_1(\mathbf{x}^{(M)}) & f_2(\mathbf{x}^{(M)}) & \cdots & f_{N_0}(\mathbf{x}^{(\mathbf{M})})\end{bmatrix} \tag{26}$$

With $\hat{\beta}$ and $\hat{\sigma}_{\text{var}}^2$ known, θ_k is found such that a likelihood function is maximized. Any values of θ_k would result in a surrogate, but the best Kriging surrogate is found by maximizing the likelihood function. For given correlation parameters p_k and θ_k, the predictor of Φ_r at an arbitrary point $\mathbf{x}$ can be shown to be

$$\hat{\Phi}_r(\mathbf{x})=\mathbf{f}^{\mathrm{T}}(\mathbf{x})\hat{\beta}+\mathbf{r}^{\mathrm{T}}(\mathbf{x})\mathbf{R}^{-1}(\mathbf{y}-\mathbf{F}\hat{\beta}) \tag{27}$$

where

$$\mathbf{r}(\mathbf{x})=[R(\mathbf{x},\mathbf{x}^{(1)})\quad R(\mathbf{x},\mathbf{x}^{(2)})\cdots R(\mathbf{x},\mathbf{x}^{(M)})]^{\mathrm{T}} \tag{28}$$

The predictor of the Kriging model given by Eq. (27) represents the optimal predictor, which results in the minimum mean square error with respect to the assumed stochastic process Φ_r. Note that the Kriging predictor is represented as an approximation to a stochastic process, but Eq. (27) is a deterministic function. Therefore, the Kriging model has been widely used in approximating deterministic computer models.

2.2.4 POD combined with surrogate model

After the LHS procedure is performed in parameter space, a total of M sampling points are produced. Then, M snapshots $\mathbf{p}^{(k)}$ are formed from the results $\mathbf{y}_{CFD}^{(k)}$ of the full order CFD computations, as shown in Fig. 5. Thus, a set of truncated POD modes and POD coefficients are obtained by snapshot matrix. To account for the ROM adaptation to the variations of multi-parameters, Kriging interpolation is performed to construct the surrogate response surfaces for POD coefficients with respect to the sampling points in multi-parameter space. Note that only one set of truncated POD modes is produced for all points in parameter space, and the Kriging interpolation is only applied to a small number of POD coefficients. Therefore, POD combined with surrogate strategy provides a very efficient construction of ROM (Xiao, 2010).

2.3 Construction of Parametric Reduced-Order Model for Unsteady Hypersonic Aerodynamics and Error Metrics

2.3.1 Construction procedure

In this paper, the developed PT-ROM for hypersonic unsteady aerodynamics features the combination of the reduction strategy for steady aerodynamic force with the unsteady component of piston theory. Thus, the PT-ROM for hypersonic unsteady aerodynamics can be written as

$$C_p^{\text{ROM}}(x,y,t)=C_{p,s}^{\text{ROM}}(x,y,t)+C_{p,\text{us}}^{\text{PT}}(x,y,t) \tag{29}$$

where

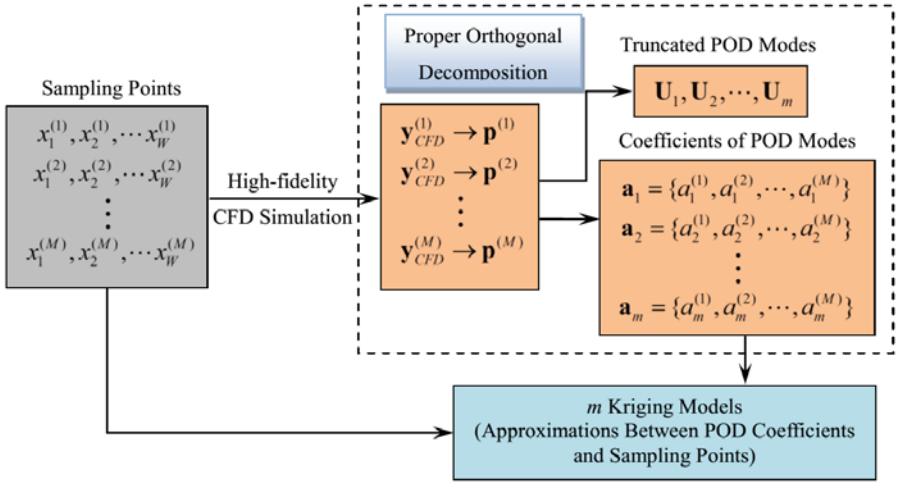

Fig. 5. Workflow of establishing the approximate relationships between POD coefficients and sampling points.

$$C_{p,us}^{\mathrm{PT}}(x,y,t)=C_{p,\mathrm{v}}(x,y,t)+\bar{C}_p(x,y,t) \tag{30}$$

Detail procedures for PT-ROM construction are summarized as follows:

(1) The input parameters (Mach number, angle of attack, etc.) with bounds are given.

(2) SLE algorithm is then used to identify a set of sampling points: $\mathbf{x}^{(k)}, k=1,2,\cdots,M$. For each sampling point, the steady-state pressure $\mathbf{p}^{(k)}$ is approximated by CFD computation prior to modification of the fluid mesh for each sample point due to the structural deformation as an input. These snapshots are collected to form the snapshot matrix $\mathbf{P}$, given by

$$\mathbf{P}=\begin{bmatrix} p_1^{(1)} & p_1^{(2)} & \cdots & p_1^{(M)} \\ p_2^{(1)} & p_2^{(2)} & \cdots & p_2^{(M)} \\ \vdots & \vdots & \ddots & \vdots \\ p_N^{(1)} & p_N^{(2)} & \cdots & p_N^{(M)} \end{bmatrix} \tag{31}$$

where N is the number of aerodynamic mesh nodes on the lifting surface.

(3) The POD modal matrix $\mathbf{U}$ is obtained by SVD for snapshot matrix $\mathbf{P}$. Form the truncated POD modes $\mathbf{U}_1,\mathbf{U}_2,\cdots\mathbf{U}_m$, $m<<M$.

(4) Compute the POD coefficients $\{\mathbf{a}^{(k)}\}|_{k=1}^{M}$. Using the truncated POD modes, the snapshot can be approximated as $\mathbf{p}^{(k)}\approx\bar{\mathbf{p}}+\sum_{i=1}^{m}a_i^{(k)}\mathbf{U}_i$.

(5) Construct Kriging response surfaces for $\{\mathbf{a}^{(k)}\}|_{k=1}^{M}$ with respect to the sampling points in parameter space.

(6) Using the surrogate model, compute the POD coefficients $\mathbf{a}^{(\mathrm{e})}$ at an arbitrary point $\mathbf{x}^{(\mathrm{e})}$ in parameter space.

(7) The vector field $\mathbf{p}^{(\mathrm{e})}$ is interpolated at an arbitrary point $\mathbf{x}^{(\mathrm{e})}$: $\mathbf{p}^{(\mathrm{e})}=\bar{\mathbf{p}}+\sum_{i=1}^{m}a_i^{(\mathrm{e})}\mathbf{U}_i$, and the steady-state pressure coefficients can then be obtained as $C_{p,s}^{ROM}=(p^{(\mathrm{e})}-p_\infty)/q_\infty$, where q_∞ is the dynamic pressure.

(8) $C_{p,us}^{\mathrm{PT}}$ is obtained by Donov's third-order piston theory. Then , compute the unsteady aerodynamics using Eq. (29).

2.3.2 Error metrics

The validation of the developed PT-ROM is performed through a comparison with the full-order CFD computations. The generalized aerodynamic force (GAF) on the surface can be defined as

$$\mathrm{GAF}=\frac{1}{2}\rho_\infty V_\infty^2\int_{\mathrm{S}}\Phi C_p\,\mathrm{dS} \tag{32}$$

where Φ is structural mode shape, and C_p is the coefficient of pressure.

Two separate error metrics are defined to evaluate the accuracy of the developed PT-ROM relative to CFD. First, the normalized root mean square error L_1 is defined as a mean absolute difference between PT-ROM and CFD results at each time step. For a simulation over T time steps, L_1 error can be written as

$$L_1=\frac{\frac{1}{T}\sum_{i=1}^{T}\left(\left|\mathrm{GAF}_{\mathrm{ROM},i}-\mathrm{GAF}_{\mathrm{CFD},i}\right|\right)}{\mathrm{Max}\left(\mathrm{GAF}_{\mathrm{CFD}}\right)-\mathrm{Min}\left(\mathrm{GAF}_{\mathrm{CFD}}\right)}\times 100\% \tag{33}$$

where $\mathrm{GAF}_{\mathrm{ROM},i}$ and $\mathrm{GAF}_{\mathrm{CFD},i}$ are PT-ROM and CFD response values at time step i , respectively.

The L_∞ error is defined as

$$L_\infty=\frac{\mathrm{Max}\left(\left|\mathrm{GAF}_{\mathrm{ROM}}-\mathrm{GAF}_{\mathrm{CFD}}\right|\right)}{\mathrm{Max}\left(\mathrm{GAF}_{\mathrm{CFD}}\right)-\mathrm{Min}\left(\mathrm{GAF}_{\mathrm{CFD}}\right)}\times 100\% \tag{34}$$

It can be seen that L_∞ error finds the maximum difference between PT-ROM and CFD results over all time steps and normalizes this quantity by the same range as in the L_1 error.

3. NUMERICAL SIMULATIONS AND DISCUSSIONS

3.1 Structural and Aerodynamic Models of the Control Surface

The planform geometric and cross-sectional views of the airfoil are shown in Fig. 6. Figure 7 shows the finite element model of control surface, which was designed by mimicking the dynamic characteristics of the F-104 Lockheed Starfighter wing. The first two natural frequencies and mode shapes of the structure are shown in Fig. 8.

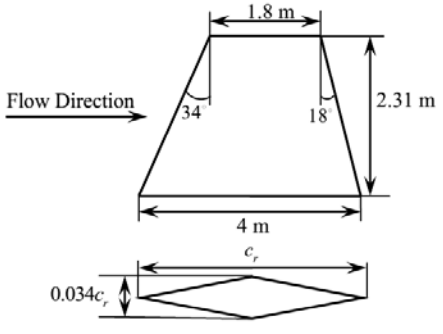

Fig. 6. Geometric model of the control surface.

As illustrated in Fig. 9, the generated CFD mesh is a vertically symmetric H-H grid with 53 points spanwise, 153 points chordwise, and 43 points extending vertically from the surface (approximately 6.1×10^5 cells). The majority of

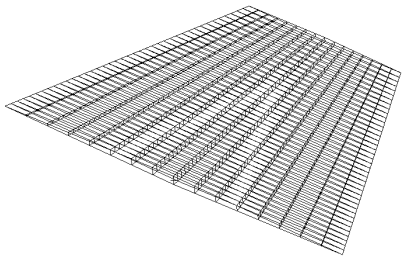

Fig. 7. Finite element model of control surface.

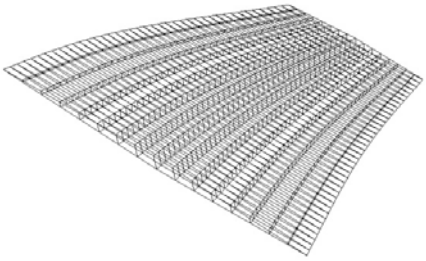

(a) Mode 1, first bending, 13.41 Hz

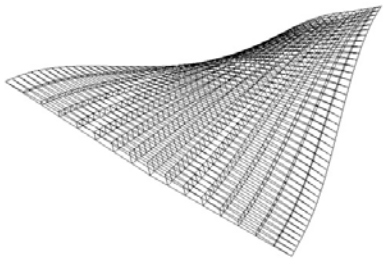

(b) Mode 2, first torsion, 37.46 Hz

Fig. 8. First two modes of control surface.

grid points are clustered near the wing surface, leading edge and mid-chord since these locations correspond to the maximum flow gradients and the boundary layers in hypersonic flows are relatively thick. This set of grid systems does not include any flow sections upstream of the wing surface since the considered flow is hypersonic and disturbances cannot propagate upstream.

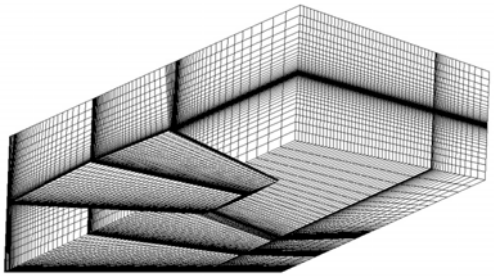

Fig. 9. Grids for full-order CFD computations.

The high-fidelity CFD solver uses an implicit, finite-volume algorithm based on upwind-biased spatial differencing to solve the Reynolds-Averaged Navier-Stokes (RANS) equations. The Menter's $k-\omega$ turbulence model is used for closure of the RANS equations. Recently, the effectiveness of this turbulence model in the hypersonic regime has been verified (Roy, 2003).

3. 2 Parameter Space And Bounds

According to the expansion theorem, the structural response can be written as a superposition of the structural modes. In this study, for simplicity, only the first two vibration modes are used to generate the structural deformation, given by

$$w(x,y,t)=a_1(t)\Phi_1(x,y)+a_2(t)\Phi_2(x,y) \quad (35)$$

where $a_1(t)$ and $a_2(t)$ are the first-order and second-order modal amplitudes, respectively. $\Phi_1(x,y)$ and $\Phi_2(x,y)$ are the first-order and second-order mode shapes, respectively.

To validate the PT-ROM adaptation to variations of multi-parameters, a total of five parameters are selected: Mach number, angle of attack, side-slip angle, and two modal amplitudes. The selected bounds for these input parameters are listed in Table 1.

Table 1 Parameter space and bounds

Parameter	Bound
Ma_∞	5 ~ 10
α	–4 deg ~ 4 deg
β	–3 deg ~ 3 deg
a_1	–0.5 ~ 0.5
a_2	–0.5 ~ 0.5

To validate the developed PT-ROM, two kinds of structural motions are specified in advance:

Deformation mode 1 (**DM1**): The structural deformation is the combination of the first two natural vibrations; that is,

$$w(x,y,t)=a_1\Phi_1(x,y)e^{i\omega_1 t}+a_2\Phi_2(x,y)e^{i\omega_2 t} \quad (36)$$

where ω_1 and ω_2 are the first-order and second-order natural frequencies, respectively, and a_1 and a_2 are specified amplitudes.

Deformation mode 2 (**DM2**): Random vibration analysis of the wing is studied, and the filtered Gaussian white noise (FWGN) excitations of the structural modes are performed.

3.3 Determination of the Number of POD Modes and the Sampling Points

The number of POD modes and the sampling points has a great impact on the accuracy of the PT-ROM framework. Therefore, the appropriate number of POD modes and sampling points is first determined to attain the best balance between the model accuracy and computational efficiency. For this purpose, 200 sampling points are generated using the SLE algorithm. Next, a total of 200 snapshots are obtained from the full-order CFD computations. Using the 200 snapshots, the snapshot matrix is assembled. After performing SVD of the covariance matrix, the POD modes are extracted. The natural logarithms for these 200 eigenvalues of the covariance matrix are given in Fig. 10. It can be seen that the flow characteristics are dominated by the lower order modes.

Further investigations on the effects of the retained

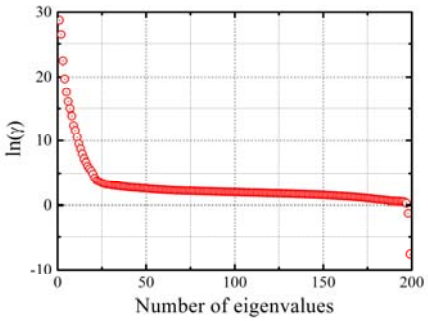

Fig. 10. Eigenvalues of the covariance matrix.

performed. To do this, a total of 20 test points in the parameter space are arbitrarily selected. The variations of the mean and the standard deviations of L_1 and L_∞ errors with increasing number of retained POD modes are shown in Fig. 11. It is clear from these results that as the number of POD modes increases, the mean and the standard deviations for both L_1 and L_∞ errors decrease rapidly until the number of POD modes exceeds 20. Hence, the first 20 POD modes are enough to characterize the flow field.

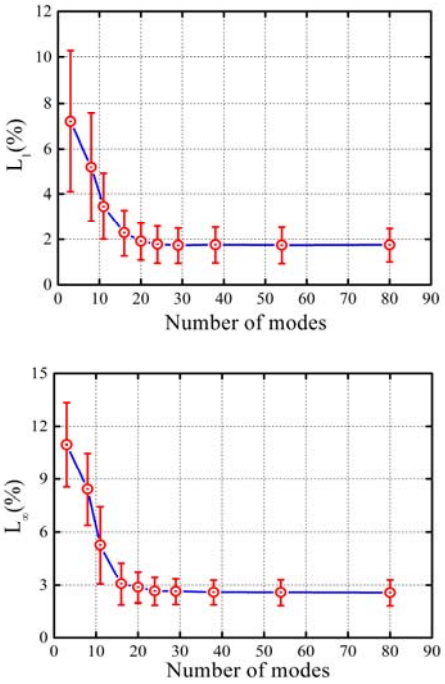

Fig. 11. Mean and standard deviations of L_1 and L_∞ errors vs the number of retained POD modes.

Next, using the first 20 POD modes, the performances of the developed PT-ROM are further evaluated by varying the number of sampling points. As shown in Fig. 12, with an increase in the number of sampling points, the mean and standard deviations of L_1 and L_∞ errors decrease rapidly until the number of sampling points exceeds approximately 200.

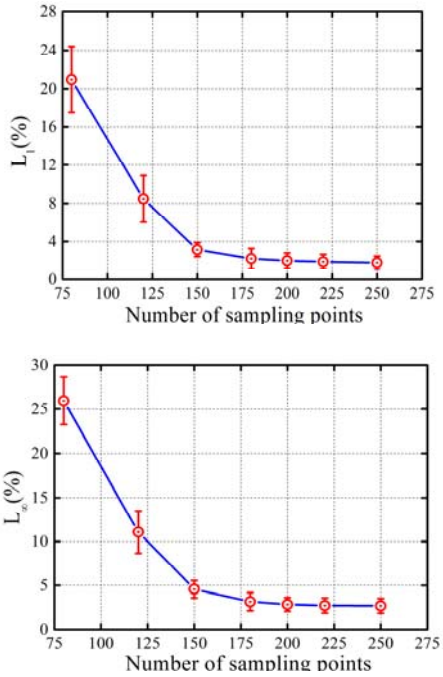

Fig. 12. Mean and standard deviations of L_1 and L_∞ errors vs the number of sampling points.

From Figs. 11 and 12, the L_1 and L_∞ errors of the PT-ROM constructing form 200 sampling points and 20 retained POD modes are less than 5%. This configuration will be used in the following simulations.

3.4 Accuracy of the PT-ROM on the Boundary of Parameter Space

The effects of Mach number on L_1 and L_∞ errors are first studied. Six Mach numbers ranging from 5 to 10 are selected for error analysis, while the other parameters remain a constant value: $\alpha = 4.0\,\text{deg}$, $\beta = 3.0\,\text{deg}$, $a_1 = 0.5$ and $a_2 = 0.5$. As shown in Fig. 13, compared with classical piston theory, the developed PT-ROM provides an excellent approximation of the full-order CFD solution, and the L_1 and L_∞ errors of PT-ROM are both less than 5%.

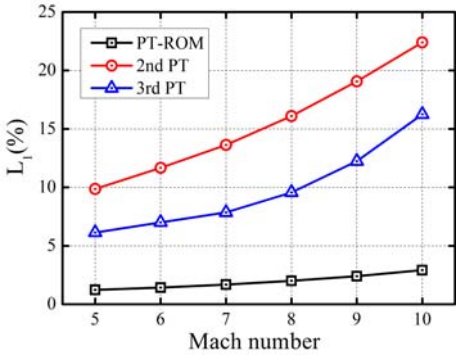

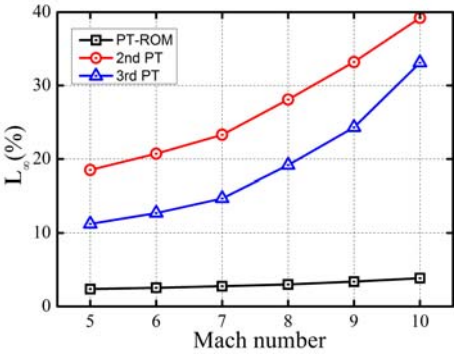

Fig. 13. L_1 and L_∞ errors vs Mach number.

Next, the accuracy of the developed PT-ROM is tested as the angle-of-attack varies. Tests are conducted at a constant Mach number, side-slip angle and oscillation amplitudes: $Ma = 10$, $\beta = 3.0\,\text{deg}$, $a_1 = 0.5$ and $a_2 = 0.5$, but at an angle-of-attack ranging from $0\,\text{deg}$ to $4\,\text{deg}$. The airfoil shape of the F-104 is symmetric, the error values at the negative angle-of-attack are simply the same as those at the positive angle-of-attack, and so only the results at the positive angle-of-attack are plotted in Fig. 14.

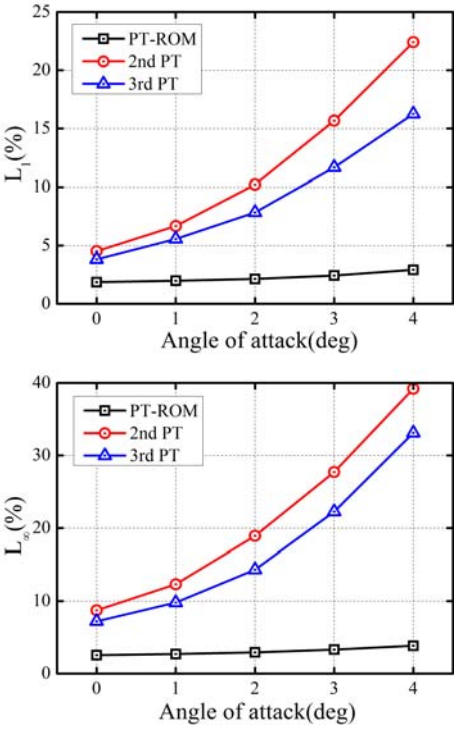

Fig. 14. L_1 and L_∞ errors vs angle of attack.

Finally, validation is performed under the condition of a constant Mach number, angle-of-attack and oscillation amplitudes, $Ma = 10$, $\alpha = 4.0\,\text{deg}$, $a_1 = 0.5$ and $a_2 = 0.5$, but with a varying side-slip angle from $-3\,\text{deg}$ to $-3\,\text{deg}$. A total of seven side-slip angles are selected for error analysis, and the results are shown in Fig. 15.

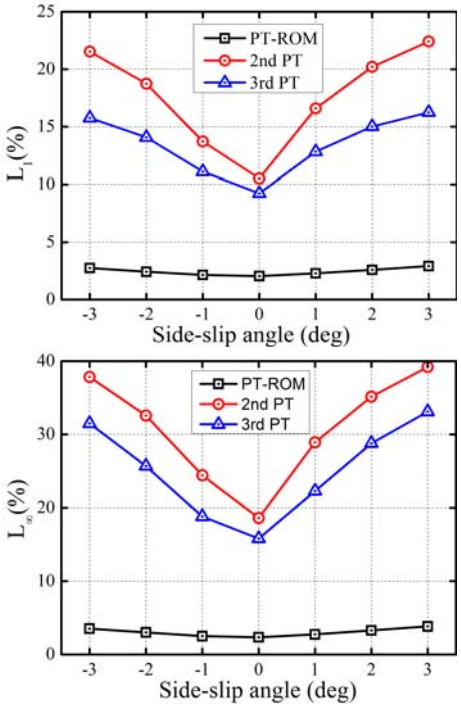

Fig. 15. L_1 and L_∞ vs side-slip angle.

From the above results, the L_1 and L_∞ errors of the PT-ROM are both less than 5% in all tests, and the accuracy of PT-ROM is greatly improved compared with the second and third-order piston theory. The PT-ROM maintains the stability of the error in the parameter space.

3.5 Validation of the Reduced-Order Aerodynamics Model

A total of 20 sampling points are arbitrarily selected for evaluating the performances of PT-ROM in multidimensional parameter space. Figures 16 and 17 show the comparison of the PT-ROM, piston theory, and CFD results for the minimum and maximum error cases, respectively. It can be seen that the steady component of the GAFs predicted by the PT-ROM agrees well with the CFD results. Since some important factors, such as the viscosity of flow, which has a primary effect on the steady component of the GAFs, cannot be considered in piston theory, as piston theory does not provide a very accurate prediction for the steady component of the GAFs. Moreover, for more complex configurations, piston theory may be fail due to its large prediction errors, whereas the PT-ROM stemming from CFD computations can be applied to any configurations.

Table 2 summarizes the statistical errors of 20 sampling points. The second-order piston theory has a lower L_1 and L_∞ error than the third-order piston theory but has a wider band of error. Among these three models, the PT-ROM exhibits the highest accuracy. It is analyzed that because of steady aerodynamic ROM joining, the complex flow phenomena in the three dimensional flow field has obtained a more accurate description.

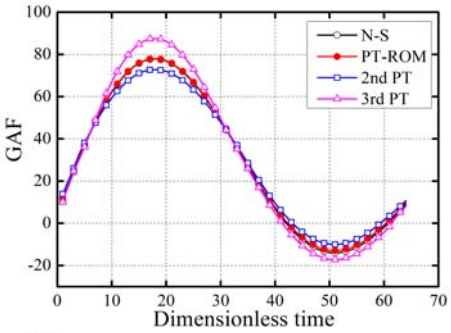

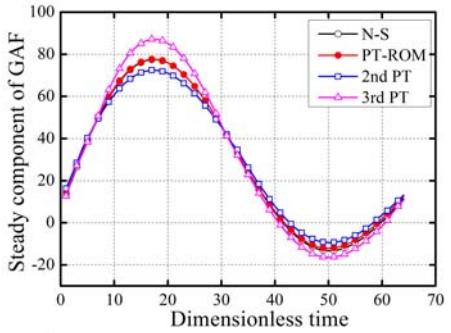

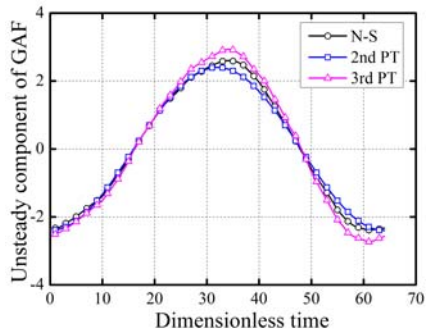

Fig. 16. Minimum error case: $Ma = 5.64$, $\alpha = -2.11\deg$, $\beta = 0.12\deg$, $a_1 = 0.46$, $a_2 = 0.41$.

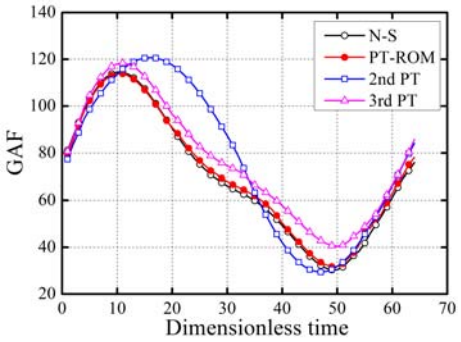

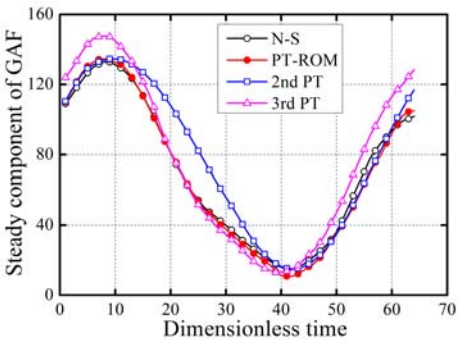

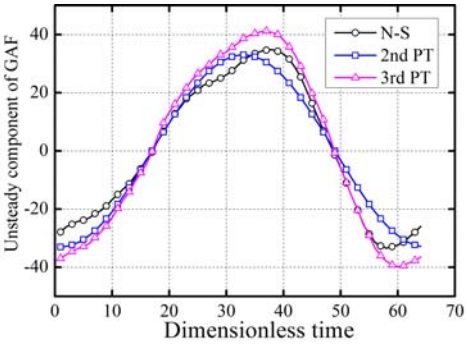

Fig. 17. Maximum error case: $Ma = 9.74$, $\alpha = 3.57\deg$, $\beta = 2.86\deg$, $a_1 = 0.47$, $a_2 = 0.35$.

Table 2 Statistical errors of GAFs

Aerodynamic model	L_1 (%)	L_∞ (%)
Second-Order Piston Theory	1.37-21.4 (Avg.11.4)	2.51-39.6 (Avg.19.8)
Third-Order Piston Theory	1.54-16.7 (Avg.9.85)	2.67-32.4 (Avg.15.1)
PT-ROM	0.92-2.87 (Avg.1.92)	1.52-3.72 (Avg.2.83)

To evaluate the effectiveness of the PT-ROM under complex structural motions, limited bandwidth filtered Gaussian white noise (FWGN) excitations are applied to the wing, and the GAFs are predicted by the PT-ROM. The FWGN excitation signals are imposed on two structural modes. The band of frequencies is limited to 0~25 Hz, and the maximal amplitudes of two structural modes are set to $a_1 = a_2 = 0.5$. First, the steady solution is computed at a given Mach number, angle-of-attack and side-slip angle: $Ma = 0.95$, $\alpha = 4\deg$, $\beta = 3\deg$. Then, this solution is used as the initial condition for unsteady computation of the aerodynamic systems subject to external structural excitations. In Fig. 18, a comparison of the GAFs shows that the developed PT-ROM is in good agreement with the direct CFD calculations. For the unsteady analysis with 1600 time steps, the computational time using PT-ROM is only 15 min, while it is 17.6 h using the full-order CFD approach. The developed PT-ROM runs several orders of magnitude faster than a full-order CFD computation while preserving a high level of accuracy.

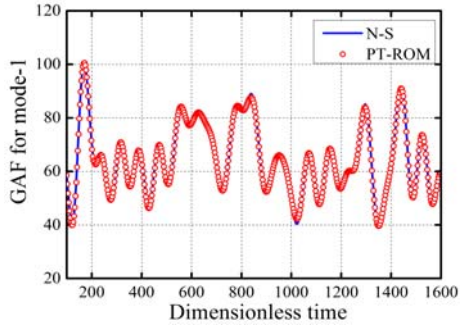

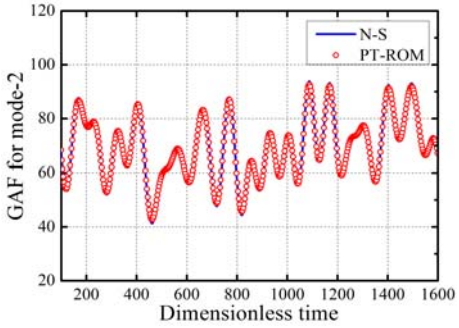

Fig. 18. PT-ROM results vs direct CFD results under FWGN excitation.

4. CONCLUSIONS

For hypersonic unsteady flow of small amplitude, the pulsation term caused by the unsteady effect is small relative to the steady component of pressure. Based on this fact, a novel ROM for hypersonic aerodynamic forces is developed, which uses POD and Kriging surrogates together for predicting the steady aerodynamic load, and the analytical expressions derived from piston theory for predicting the unsteady part. The numerical results demonstrate that the GAFs computed by using the PT-ROM agree well with those from direct CFD computations. Due to the capability of capturing the complex flow phenomena, the PT-ROM provides a higher accuracy than the traditional piston theory. Since steady CFD computations are only required to extract the POD bases, a significant reduction in computational time is achieved compared with unsteady CFD computations. Furthermore, the PT-ROM also exhibits a successful ROM adaptation to the variation of more than two flight parameters. This means that there is no need to reconstruct the ROM with flight parameters changing. Once the PT-ROM is constructed, it can be efficiently used for various aeroelastic analyses. For aeroelastic analysis of the hypersonic vehicle, the coupling with the thermal problem is an important aspect of the problem, which will be considered for further application of the proposed ROM approach.

ACKNOWLEDGEMENTS

This study was supported by the National Natural Science Foundation of China under Grant No. 11472128.

REFERENCES

Amsallem, D. and C. Farhat (2008). Interpolation method for adapting reduced-order models, *AIAA J.* 46 (7) 1803-1813.

Ashkey, H. and G. Zartarian (1956). Piston theory: a new aerodynamic tool for the aeroelastician. *Journal of the Aeronautical Sciences* 23 (12) 1109–1118.

Benner, P., S. Gugercin and K. Willcox (2013). A survey of model reduction methods for parametric systems. *SIAM Review* 57 (4) 483-531.

Boulahia, A., S. Abboudi and M. Belkhiri (2014). Simulation of viscous and reactive hypersonic flows behaviour in a shock tube facility: TVD schemes and flux limiters application. *Journal of Applied Fluid Mechanics* 7 (2) 315-328.

Dowell, E. H. (2016). Far Field Predicted by Piston Theory. *AIAA J.* 54 (1) 364-366.

Donov, A. E. (1956). A flat wing with sharp edges in a supersonic stream. *National Advisory Committee for Aeronautics, Washington, DC, United States, 1956.*

Gupta, K. K. and M. C. Bach (2007) Systems identification approach for a computational-fluid-dynamics-based aeroelastic analysis. *AIAA J.* 45 (12) 2820-2827.

Ghoreyshi, M., A. Jirásek and R. M. Cummings (2014). Reduced order unsteady aerodynamic modeling for stability and control analysis using computational fluid dynamics. *Progress in Aerospace Science* 71 167-217.

Glaz, B., L. Liu and P. P. Friedmann (2010). Reduced-order nonlinear unsteady aerodynamic modeling using a surrogate-based recurrence framework. *AIAA J.* 48 (10) 2418-2429.

Huang, R., H. Y. Hu and Y. H. Zhao (2014). Nonlinear reduced-order modeling for multiple-input / multiple-output aerodynamic systems. *AIAA J.* 52 (6) 1219-1231.

Hall, K. C., J. P. Thomas and E. H. Dowell (2000). Proper orthogonal decomposition technique for transonic unsteady aerodynamic flows. *AIAA J.* 38 (10) 1853-1862.

Kim, T. (2015). Surrogate model reduction for linear dynamic systems based on a frequency domain modal anaylsis. *Compute Mechanics* 56 (4) 709-723.

Lucia, D. J., P. S. Beranm and W. A. Silva (2004). Reduced-order modeling: new approach for computational physics. *Progress in Aerospace Science* 40 51-117.

Liu, D. D., Z. X. Yao, D. Sarhaddi and F. Chavez (1997). From piston theory to a unified hypersonic-supersonic lifting surface method. *Journal of Aircraft* 34 (3) 304-312.

Lieu, T. and C. Farhat (2007). Adaptation of aeroelastic reduced-order models and application to an F-16 Configuration. *AIAA J.* 45 (6) 1244-1257.

Liu, H. J., Y. H. Zhao, and H. Y. Hu (2016). Adaptive flutter suppression for a fighter wing via recurrent neural networks over a wide transonic range. *International Journal of Aerospace Engineering* 2016 1-9.

Lieu, T. and M. Lesoinne (2004). Parameter adaptation of reduced order models for three-dimensional flutter analysis. *42nd AIAA*

Aerospace Sciences Meeting and Exhibit, Reno, Nevada, 2004.

McNamara, J. J. and P. P. Friedmann (2011). Aeroelastic and aerothermoelastic analysis in hypersonic flow: past, present, and future. *AIAA J*. 49 (6) 1089-1122.

McNamara, J. J., P. P. Friedmann, K.G. Powell, B.J. Thuruthimattam and R.E. Bartels (2008). Aeroelastic and aerothermoelastic behavior in hypersonic flow. *AIAA J*. 46 (10) 2591-2610.

McNamara, J. J., A. R. Crowell, P. P. Friedmann, B. Glaz and A. Gogulapti (2010). Approximate modeling of unsteady aerodynamics for hypersonic aeroelasticity. *Journal of Aircraft* 47 (6) 1932-1945.

Mackay, M. D., R. J. Beckman and W. J. Conover (2000). A comparison of three methods for selecting values of input variables in the analysis of output from a computer code. *Technometrics* 42 (1) 55-61.

Roy, C. J. and F. G. Blottner (2003). Methodology for turbulence model validation: application to hypersonic flows. *Journal of Spacecraft and Rockets* 40 (3) 313-325.

Skujins, T. and C. E. S. Cesnik (2011). Reduced-order modeling of hypersonic unsteady aerodynamics due to multi-modal oscillations. *17th AIAA International Space Planes and Hypersonic Systems and Technologies Conference, San Francisco, California, 2011*.

Schmidt, R. F. and M. N. Glauser (2004). Improvements in low dimensional tools for flow-structure interaction problems: using global POD. *42nd AIAA Aerospace Sciences Meeting and Exhibit, Reno*, Nevada, 2004.

Scott, R. C. and A. S. Pototzky (1996). Quasisteady aerodynamics for flutter analysis using steady computational fluid dynamics calculations, *Journal of Aircraft* 33 (1) 191-197.

Skujins, T. and C. E. S. Cesnik (2014). Reduced-order modeling of unsteady aerodynamics across multiple mach regimes. *Journal of Aircraft* 51 (6) 1681-1704.

Thomas, J. P., E. H. Dowell, and K. C. Hall (2010). Using automatic differentiation to create a nonlinear reduced-order-model aerodynamic solver. *AIAA J*. 48 (1) 19-24.

Xiao M., P. Breitkopf，R. F. Coelho，C. Knopf-lenoir，M. Sidorkiewicz and P. Villon (2010) Model reduction by CPOD and Kriging. *Structural & Multidisciplinary Optimization* 41(4) 555-574.

Zhu, H. G., L. Liu, T. Long and L. Peng (2012). A novel algorithm of maximin latin hypercube design using successive local enumeration. *Engineering Optimization* 44 (5) 551-564.